"Imaging coherent transport in a mesoscopic graphene ring"

Cabosart, Damien ; Faniel, Sébastien ; Rodrigues Martins, Frederico ;
Brun, Boris ; Felten, Alexandre ; Bayot, Vincent ; Hackens, Benoît

Abstract

Mesoscopic graphene devices often exhibit complex transport properties, stemming both from the peculiar electronic band structure of graphene and from the high sensitivity of transport to local disorder in this twodimensional crystal. To disentangle contributions of disorder in the different transport phenomena at play in such devices, it is necessary to devise new local-probe methods and to establish links between transport and the microscopic structure of the devices. Here, we present a spatially resolved investigation of coherent transport inside a graphene quantum ring (QR), where Aharonov-Bohm conductance oscillations are observed. Thanks to scanning gate microscopy (SGM), we first identify spatial signatures of the Coulomb blockade, associated with disorder-induced localized states, and of charge-carrier interferences. We then image resonant states which decorate the QR local density of states (LDOS). Simulations of the LDOS in a model disorder graphene QR and temperature depen...

Document type : *Article de périodique (Journal article)*

Imaging coherent transport in a mesoscopic graphene ring

Damien Cabosart,[1,*] Sébastien Faniel,[1] Frederico Martins,[1] Boris Brun,[2] Alexandre Felten,[3] Vincent Bayot,[1] and Benoit Hackens[1,†]

[1]*Université catholique de Louvain, Institute of Condensed Matter and Nanosciences (IMCN/NAPS), B-1348 Louvain-la-Neuve, Belgium*

[2]*Institut Néel, Université Grenoble Alpes, 38042 Grenoble, France*

[3]*University of Namur, Research Center in Physics of Matter and Radiation (PMR), B-5000 Namur, Belgium*

(Received 10 July 2014; revised manuscript received 3 November 2014; published 25 November 2014)

Mesoscopic graphene devices often exhibit complex transport properties, stemming both from the peculiar electronic band structure of graphene and from the high sensitivity of transport to local disorder in this two-dimensional crystal. To disentangle contributions of disorder in the different transport phenomena at play in such devices, it is necessary to devise new local-probe methods and to establish links between transport and the microscopic structure of the devices. Here, we present a spatially resolved investigation of coherent transport inside a graphene quantum ring (QR), where Aharonov-Bohm conductance oscillations are observed. Thanks to scanning gate microscopy (SGM), we first identify spatial signatures of the Coulomb blockade, associated with disorder-induced localized states, and of charge-carrier interferences. We then image resonant states which decorate the QR local density of states (LDOS). Simulations of the LDOS in a model disorder graphene QR and temperature dependence of SGM maps confirm the presence of such scarred states.

DOI: 10.1103/PhysRevB.90.205433 PACS number(s): 72.80.Vp, 73.23.−b

I. INTRODUCTION

The term "coherent electron transport" encompasses a broad range of physical phenomena involving interferences between electron wave packets propagating in complex media and nanostructures. In the mesoscopic regime, i.e., when the size of the measured device is comparable to the electron phase coherence length (L_ϕ), fluctuations are observed in the device electrical conductance, originating from multiple-path interferences as charge carriers are scattered by impurities (in disordered systems [1]) or by device boundaries (in ballistic systems [2]). In this regime, simulations predict that, even in the case of chaotic geometries, stable "semiclassical orbits" take place inside mesoscopic devices due to charge-carrier collimation from the leads [3]. In that case, the wave-function amplitude is concentrated along particular resonant structures whose geometry can be tuned, e.g., by changing the device geometry or the magnetic field [2]. Such fluctuations in the wave functions, or "scars," have also been described analytically in the case of disordered metallic systems [4]. Experimental probes of these resonant structures are not limited to macroscopic (magneto)conductance measurements. Indeed, real-space imaging of the scarred local density of states (LDOS) was realized in ballistic devices thanks to scanning gate microscopy (SGM) [5–7], a technique based on mapping the device conductance while scanning an electrically biased nanotip in its vicinity [8].

Stimulated by the large interest for the exceptional electronic properties of graphene [9], SGM was also recently used to investigate transport in mesoscopic devices carved from this two-dimensional carbon crystal. However, from SGM data on graphene constrictions, it was found that localized states are ubiquitous in most mesoscopic graphene devices, and can be imaged in SGM thanks to Coulomb blockade (CB) effects, tuned by the tip-induced perturbation [10–12]. Localized states are associated with defects and inhomogeneities in the charge density (e.g., the presence of electron and hole puddles [13,14]). They were found to be so dominant in determining the transport properties of real mesoscopic graphene devices that it was only possible in rare cases to realize SGM imaging of two carrier-interference effects—weak localization (WL) [15] and universal conductance fluctuations (UCFs) [16,17]—both related to the presence of defects. However, no signs of scarred states could be evidenced in SGM images in the UCFs or WL regimes. But the phenomenology of coherent transport in graphene is much richer than UCFs and WL. For example, the magnetic and electrostatic Aharonov-Bohm (AB) effects [18–23] have already been examined using conventional transport measurements. Moreover, a significant number of questions recently emerged about the physics of some—observed or predicted—peculiar phenomena such as the increase of the AB oscillation amplitude at high magnetic field [18], the stability of semiclassical orbits with respect to system boundaries [24], the possibility to observe "relativistic quantum scars" in the LDOS of mesoscopic graphene devices [25,26], and the non-ergodicity of UCFs in disordered mesoscopic graphene [27]. Revisiting these questions using the SGM imaging technique would certainly help to understand the underlying physics.

In this paper, we investigate spatially resolved low-temperature electronic transport within a graphene quantum ring (QR) laterally defined by fluorination. First, we analyze the origin of conductance fluctuations observed when applying a magnetic field perpendicular to the plane of the QR and find clear signatures of the AB effect. Thanks to SGM mapping, we find that transport through the QR is more rich and complex than what could be inferred from conventional transport experiments. We identify regions where localized states dominate transport inside the structure, and separate their contribution from spatial signatures of charge-carrier interferences. Moreover, radial conductance fringes observed in the SGM maps of QR arms are ascribed to the presence

*damien.cabosart@uclouvain.be

†benoit.hackens@uclouvain.be

of resonant structures scarring the LDOS. Support for the presence of such scars is found in the T dependence of SGM maps, and from tight-binding simulations of the LDOS in a graphene QR with a similar aspect ratio, including a random disorder potential.

II. DEVICE FABRICATION

The device examined in this work was fabricated from a monolayer graphene flake, obtained by mechanical exfoliation of natural graphite and transferred on a doped silicon wafer covered with a thermally grown 90-nm-thick dioxide layer. Optical contrast with the substrate and micro-Raman spectroscopy were used to confirm the presence of graphene monolayers. We then used electron-beam lithography (EBL) for patterning a polymethyl methacrylate (PMMA) layer spin coated on top of the substrate, and proceeded with a metal deposition [Ti (5 nm)/Au (30 nm)] and liftoff to define electrical contacts to the graphene device. A second EBL, followed by a CF_4 plasma process [28], allowed us to define the QR geometry by fluorination of the graphene areas that were not covered by the PMMA resist. The fluorination consists in creating covalent sp^3 bonds between carbon atoms in the graphene lattice and fluorine atoms [29–32], which opens a band gap of up to 3 eV in the fluorinated areas [30,33]. Combining EBL patterning and fluorination, it is therefore possible to define electrically conductive pathways and form graphene-based devices [34]. Dashed lines on the atomic force microscope (AFM) image of the QR [Fig. 1(a)] delineate the fluorinated areas. The QR outer and inner radii are ∼400 and 200 nm, respectively. Moreover, micro-Raman spectroscopy mapping has been used to confirm the synthesis of fluorinated graphene in the designated areas [35]. Mechanical cleaning with an AFM tip in contact mode was performed in the QR region and in its vicinity, to remove residues from the fabrication process [36].

III. EXPERIMENTAL METHOD

The QR conductance G was measured in vacuum, using a four-contact low-frequency (17.5 Hz) lock-in technique, with a source-drain bias voltage always kept below k_BT/e (k_B is the Boltzmann constant, and e is the electron charge). The magnetic field B is applied perpendicular to the plane of the device, and in the present experiment we always ensured that the charge-carrier cyclotron radius was larger than the QR arms' width (weak magnetic field limit). Varying the voltage V_g applied on the backgate formed by the doped silicon wafer allows us to tune the carrier density (n) in the graphene device. G maps were obtained using a home-made SGM system in a ^{3}He-^{4}He dilution refrigerator, down to a temperature $T = 30$ mK. The SGM system uses a metal-coated Si cantilever glued on a quartz tuning fork [37]. First, the corners of electrical contacts, used as alignment marks, located at a distance of ∼1 μm from the QR, are scanned in AFM mode. The tip is then lifted from the surface and positioned above the QR. This alignment is based on high-resolution AFM maps obtained at room temperature, so that the tip does not scan over the device in AFM mode at low T. Finally, a voltage V_{tip} is applied on the tip.

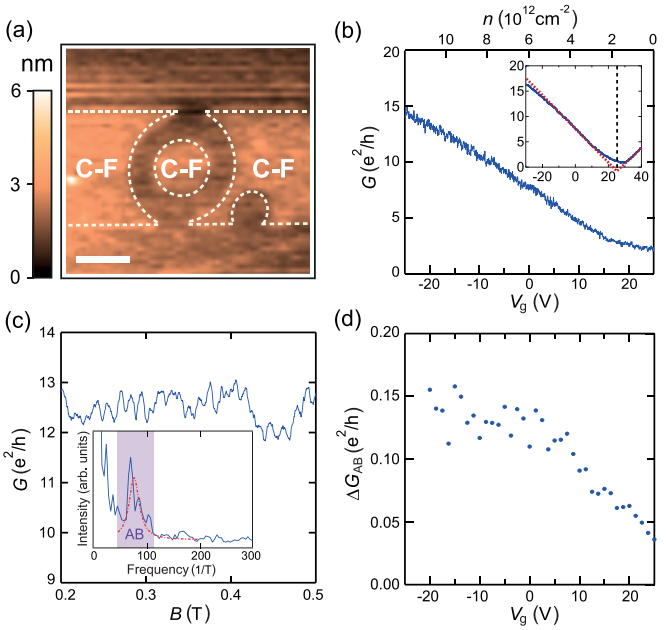

FIG. 1. (Color online) Structural characterization of the QR and electrical transport measurements. (a) AFM picture of the QR. Dashed lines delineate fluorinated graphene regions. The scale bar is 400 nm. (b) G vs V_g at 30 mK. The inset presents G vs V_g at 7 K. The position of the Dirac point is ∼25 V, as determined by linear fits performed on both sides of the minimum (red dashed lines). (c) Magnetoconductance obtained at 30 mK and $V_g = -15$ V. The inset represents the FFT of the magnetoconductance curve. The shaded region indicates the AB frequency range defined by the outer and inner radii of the ring. The red dashed line is a Lorentzian fit to the data. (d) AB oscillations amplitude as a function of V_g.

For SGM imaging, the tip scans at a constant distance ∼80 nm from the surface while recording the QR conductance G.

IV. CONVENTIONAL TRANSPORT MEASUREMENTS

Figure 1(b) shows G versus (vs) V_g, measured at $T = 30$ mK. The position of the neutrality point in G vs V_g is ∼ 25 V, as inferred by complementary G vs V_g data obtained at higher T [see inset of Fig. 1(b)]. Therefore, in the V_g range considered in Fig. 1(b), p-type carriers dominate transport. Note that p-type doping has been reported in graphene nanoribbons defined by a similar fluorination process [34], and was attributed to the different work functions between pristine and fluorinated graphene.

A hole mobility of ∼1000 cm^2/V s can be estimated from a linear fit to the data in Fig. 1(b) in the V_g range between −15 and +15 V. Note that, for the whole range of V_g investigated in this work, the regime of charge transport inside the QR is diffusive, since the carrier mean free path (L_μ) is much smaller than the QR typical dimensions (L_μ ∼ 20–30 nm in the V_g range between −15 and +15 V). Superimposed on the downward trend of G as V_g increases, reproducible fluctuations of G vs V_g can be noticed in Fig. 1(b). Such fluctuations are commonly observed in laterally confined graphene devices, and can be ascribed to carrier interference effects (i.e., the UCFs [38]), which are modulated by V_g-induced changes of

the Fermi energy, or to Coulomb charging of small localized states within the graphene sheet [39–41].

Figure 1(c) shows that the QR magnetoconductance at 30 mK and $V_g = -15$ V exhibits periodic oscillations, which decorate a broad aperiodic background. They are signatures of B-induced phase shifts between charge-carrier partial waves transmitted through both arms of the QR, i.e., the Aharonov-Bohm effect. The Fourier transform of the magnetoconductance is presented in the inset of Fig. 1(c), and exhibits a peak centered around 72.5 T^{-1} [the peak position is extracted from a Lorentzian fit to the data—see the red dashed line in the inset of Fig. 1(c)]. This frequency corresponds to a period of 13.8 mT, expected for h/e-periodic AB oscillations associated with circular carrier trajectories with a radius ∼310 nm, in good agreement with the average lithographic radius of the QR. This observation indeed confirms that fluorinated areas are electrically insulating, and effectively delimitate the graphene QR.

AB oscillations are observed for a large range of backgate voltage, from $V_g = -20$ V (far from the Dirac point) to $V_g = +25$ V (close to the Dirac point). However, the amplitude of AB oscillations (ΔG_{AB}) is not constant when approaching the Dirac point, as illustrated in Fig. 1(d), but shows an almost linear decrease in the range of 0 and +25 V. The vanishing amplitude of AB oscillations close to the Dirac point is a peculiar feature of the AB effect in graphene QRs [18], and may be related to a spatially inhomogeneous carrier density within the QR [42].

V. SCANNING GATE MICROSCOPY MEASUREMENTS

To explore charge transport at the local scale inside the QR, we then perform SGM imaging. The setup for SGM is schematically represented in Fig. 2(a). As the microscope tip is voltage biased, charge carriers inside the device experience a local tip-induced electrostatic perturbation. This causes a change in their transmission, which can be measured by mapping G as the tip position moves in a plane parallel to the device plane. A SGM map of G near the QR is shown in Fig. 2(b) for $V_{tip} = -2$ V, $V_g = -5$ V, and $B = 30$ mT (the continuous lines delineate the position of the QR). Spatial conductance fluctuations, or conductance fringes, are observed. The fringes are not limited to the area of the QR, as also observed in the case of SGM images of semiconductor quantum rings [43], because of the lateral extent of the tip-induced perturbation. The width of SGM fringes is typically approximately tens of nm to ∼100 nm for this experimental configuration [see red dashes highlighting two examples of G fringes in Fig. 2(b)].

At lower charge density, the pattern of SGM fringes changes, and the standard deviation of the electrical conductance in the overall SGM mapping decreases, as shown by the comparison between Figs. 2(b) and 3(a), obtained for $V_g = -5$ and +18 V, i.e., $n = 7.2 \times 10^{12}$ cm^{-2} and 1.6×10^{12} cm^{-2}, respectively, and $V_{tip} = -2$ V. This trend is similar to that of the AB oscillations' amplitude, which already points toward a coherent origin of the SGM features [Fig. 1(d)].

A. Coulomb blockade

Increasing the temperature to $T = 500$ mK, one obtains the SGM map displayed in Fig. 3(b) for $V_g = +18$ V. We

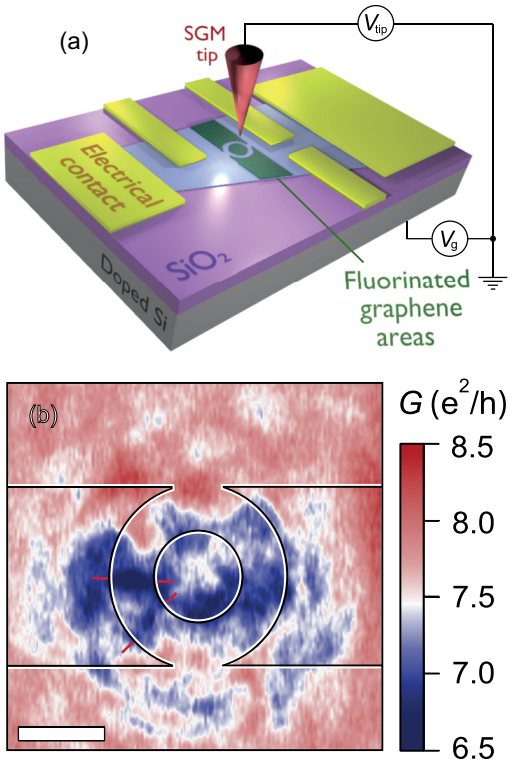

FIG. 2. (Color online) SGM imaging of the QR. (a) SGM experimental setup: the graphene QR is defined by fluorination (green regions) and lies on an oxidized doped Si substrate, used as a back gate. The yellow areas correspond to ohmic contacts on top of the graphene flake. A metallic tip is approached close to the QR, with an applied bias V_{tip}, and is scanned to produce a SGM map of the device conductance. (b) SGM conductance map obtained at large charge-carrier concentration ($n = 7.2 \times 10^{12}$ cm^{-2}; $V_g = -5$ V), $V_{tip} = -2$ V, $B = 30$ mT, and $T = 30$ mK. The continuous lines delineate the position of the QR. The red dashes highlight two examples of conductance fringes inside the QR arms. The scale bar represents 400 nm.

note several changes in the SGM contrast, with respect to the SGM image measured with the same backgate and tip biases at $T = 30$ mK [Fig. 3(a)]. In particular, the overall amplitude of the fringes decays, and most of the SGM fringes with a small characteristic length decay or vanish, especially at the left and right sides of the QR. This leaves a simpler pattern of SGM fringes at higher temperature, so that the spatial movement of the remaining features in SGM maps can be tracked more easily in the V_{tip} dependence of the linescan AA′ [green dashed line in Fig. 3(b)], shown in Fig. 3(c).

In the plot of Fig. 3(c), different sets of Gaussian-like curves can be identified, formed by bright fringes with a curvature depending on the sign of V_{tip}, and centered on different parts of the device [note that parabolic or Lorentzian curves can also fit the data in Fig. 3(c)—more data would be needed to precisely identify the curve shape]. Such curves have already been observed in the case of scanning gate experiments on open graphene constrictions [12]. They are related to the presence of multiple localized states located along the device, accidentally produced by disorder which induces charge inhomogeneity in the device, and tunnel-coupled to the transmitted channels.

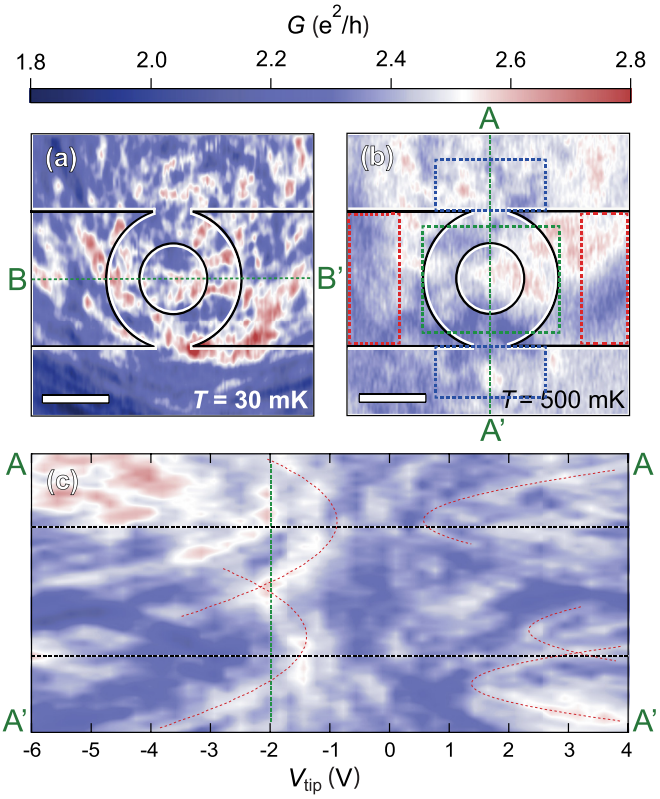

FIG. 3. (Color online) SGM images of the QR at low charge-carrier density, close to the neutrality point. (a),(b) SGM map at $V_g = +18$ V, $B = 0.7$ T, $V_{tip} = -2$ V, and $T = 30$ and 500 mK, respectively. Continuous lines indicate the position of the QR. The scale bars correspond to 400 nm. (c) Plot of the conductance vs V_{tip} and the tip position along the AA′ green dashed line in Fig. 3(b). The positions of both QR apertures are given by the black dashed lines. Red dashed lines correspond to a Gaussian fit to the data, and highlight Coulomb resonances.

Approaching the tip to a dot or changing the tip voltage causes the individual confinement-induced energy levels inside each localized state to be shifted. Each time the energy is equal for two different numbers of charge carriers in the localized state, charge carriers can be transmitted through the localized state, which therefore constitutes a new channel for charge-carrier transmission. In that case, the conductance increases and a Coulomb blockade peak is observed in the conductance. For a given dot and at fixed tip height, lines of constant dot potential correspond to Gaussian-like curves in a plot where the tip position and voltage are varied, so that each bright Gaussian-like curve in Fig. 3(c) corresponds to a CB peak. As already pointed out in previous works [44], the position of the extremum of these isopotential lines allows us to infer the location of the QDs. From data in Fig. 3(c), one can then conclude that the active QDs are predominantly located close to the QR openings. Moreover, away from the CB peaks (in the CB valleys), $G \sim 2.2$–$2.4\ e^2/h$ in Fig. 3(c). This means that transport in the QR occurs through open transmitting channels, in parallel with Coulomb-blockaded channels. When these CB channels are transmitting, G increases up to $\sim 2.6\ e^2/h$; i.e., their contribution is far from negligible.

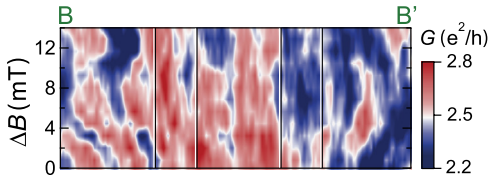

FIG. 4. (Color online) SGM line profile, measured along the BB′ green dashed line in Fig. 3(a), as a function of the magnetic field ($V_{tip} = -2$ V, $V_g = +18$ V and $B = 0.7$ T). Vertical lines correspond to the inner and outer limits of the QR.

B. Electrostatic Aharonov-Bohm effect

At this point in the analysis, one can already say that charge-carrier interference effects (AB oscillations) and the Coulomb blockade (in SGM data at low carrier density) contribute to transport in the QR. The question is then, can we identify the signatures of coherent transport in SGM images?

To address this question, we first examine the B dependence of the SGM fringes at $T = 30$ mK, and observe their spatial evolution. Figure 4 shows the B dependence of the SGM line profile BB′ crossing the QR area [see Fig. 3(a)]. SGM fringes observed on the left and right sides of the QR are shifting in opposite directions as the magnetic field is tuned, contrary to the fringes observed in the central part of the QR, which are not moving. Moreover, the range of magnetic field periodicity that can be estimated for the fringes observed outside the QR area copes with the range of acceptable periods for an AB effect involving semiclassical trajectories orbiting around the QR. One can therefore ascribe the SGM observations on both sides of the QR to a tip-induced electrostatic AB effect, mixed with UCFs, which have similar amplitudes [this can also be observed in the magnetoresistance curve in Fig. 1(c)]. Since UCFs exhibit a random evolution with B, the left-right symmetry is broken in Fig. 4. A similar behavior (a tip-modulated AB effect) has already been observed in semiconductor QRs [43].

C. Quantum scars

After examining fringes located mostly outside the QR area, we now focus on the SGM contrast observed when the tip scans over the QR area. From the Gaussian-like curves observed in Fig. 3(c), we deduced that CB is involved in at least part of the contrast observed in SGM. However, part of the fringes in Fig. 3(c) do not follow a Gaussian-like movement when changing V_{tip}, in particular around $V_{tip} = 0$ V. Moreover, increasing charge-carrier density should reduce the contribution from localized states in the device conductance. A SGM image measured at $V_g = -5$ V and $V_{tip} = +0.5$ V is shown in Fig. 5(a). In these imaging conditions, the conductance map in the region of the QR arms is decorated with radial fringes [some of them are highlighted by arrows in Fig. 5(a)]. The fringes are not uniformly distributed along the circumference of the QR, but rather generate an asymmetric pattern inside the QR arms. Note also that, even though the imaging conditions are different, a very similar fringe pattern is also observed in Fig. 3(a), and radial fringes with a different distribution are also visible in Fig. 2(b). Such radial fringes are reminiscent of previous SGM observations in semiconductor quantum

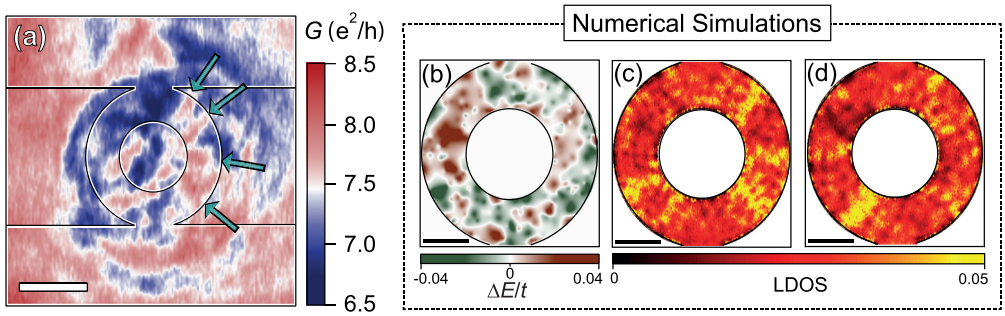

FIG. 5. (Color online) SGM mapping and LDOS simulations at large charge-carrier density. (a) SGM map at $V_g = -5$ V, $B = 30$ mT, $V_{tip} = +0.5$ V, and $T = 30$ mK. Continuous lines indicate the position of the QR. Arrows point toward radial fringes inside the QR. The scale bar corresponds to 400 nm. (b) QR model geometry used for tight-binding simulations including a random disorder potential. (c),(d) LDOS simulations for $E_F/t = 0.144$ and 0.119, respectively. For each figure, the black scale bar represents $100a$.

rings [6,43]. Simulations yielded similar radial fringes patterns for the local density of states (LDOS) in mesoscopic QRs incorporating charged defects in the confining potential, and showed the correspondence between simulated LDOS and simulated SGM images when the electrostatic perturbation induced by the SGM tip is small enough [6,45]. The radial fringes in Fig. 5(a) therefore represent a hint that the same behavior is observed in the diffusive graphene QR examined here, and that semiclassical orbits scarring the LDOS are actually imaged in this SGM experiment.

To examine whether such scarred states could be observed in a graphene QR, we computed the LDOS in the model geometry shown in Fig. 5(b). The QR inner and outer radii are $100a$ and $200a$, respectively, where a is the graphene lattice constant. In order to get closer to the real measured QR, we included a random disorder potential forming electron and hole puddles in the vicinity of the Dirac point [see Fig. 5(b)]. Local energy fluctuations are scaled to realistic values considering [14], where the authors directly measure disorder-induced variations in the electrostatic potential in a graphene monolayer on SiO_2, using scanning tunneling spectroscopy. We included a similar random disorder potential in our numerical model, i.e., with a comparable energy fluctuation amplitude ($\Delta E/t$, where t is the hopping energy) and correlation length.

Numerical calculations of the LDOS were performed with the KWANT package based on tight-binding models [46]. All simulations were computed in a low-energy regime (i.e., $E_F/t \ll 1$, where E_F is the Fermi energy), so that a qualitative comparison with the SGM map in Fig. 5(a) is valid [6,47]. The LDOS simulations for $E_F/t = 0.144$ and 0.119 are plotted in Figs. 5(c) and 5(d), respectively [48]. As on the SGM image in Fig. 5(a), radial fringes scar the LDOS producing an asymmetric pattern originating from the disorder potential. Note that the pattern of scars is sensitive to the value of the Fermi energy, and it is quite common to observe radial scars in this geometry, as previously shown in the case of semiconductor quantum rings, even when a small charged impurity density was included in the simulation [45]. Our simulations show that radial scars persist even in the case of a graphene QR with a much larger relative charged impurity density. It therefore makes sense to ascribe the radial SGM fringes in Fig. 5(a), measured on a QR with a mean free path much smaller than the QR arms' width, to radial quantum scars in the LDOS. Note that radial SGM fringes are also visible in Figs. 2(b) and 3(a), measured using different tip polarization parameters. It is also worth noting that radial fringes in our simulated LDOS are equally robust even after incorporating corrugation effects induced by the SiO_2 substrate in our model graphene QR [49,50].

VI. TEMPERATURE DEPENDENCE

To further test the interpretation of each feature in SGM images, we now examine the T dependence of the SGM rms contrast ΔG_{SGM} calculated over distinct regions, identified by the dashed lines in Fig. 3(b). Figure 6 shows that ΔG_{SGM} exhibits a power-law decay with the temperature $\Delta G_{SGM} \sim T^p$ with $p = -1/2$, when the tip scans over the fluorinated areas on the sides of the QR [regions enclosed in the red squares in Fig. 3(b)] where the SGM pattern is consistent with probing the electrostatic AB effect. The same exponent $p = -1/2$ is observed for the rms amplitude of the AB oscillations in the magnetoconductance of our sample (for $V_g = +25$ V) even though a slightly faster decay is observed above ~300 mK, as discussed below. Such a value for p is typical for the AB oscillations in diffusive QRs, as reported experimentally in the case of metallic QRs [51,52] and etched graphene QRs [18]. The observed exponent p, and similarity of both temperature dependences, confirm that, when the tip scans on the sides of the QR's arms, the SGM tip-induced perturbation tunes charge-carrier interferences inside the QR [53].

When governed by the thermal averaging, the evolution with temperature of ΔG_{AB} in a metallic ring is given by the formula [54]

$$\Delta G_{AB} = C\frac{e^2}{h}\frac{L_T}{\pi r}\left(\frac{L_\phi}{\pi r}\right)^{1/2}\exp\left(-\frac{\pi r}{L_\phi}\right), \qquad (1)$$

where C is a geometrical parameter close to 1, e is the elementary charge, h is the Planck constant, r is the radius of the ring, and L_T is the thermal diffusion length. Note that a rigorous treatment of energy transfers along the ring circumference leads to a slightly different form for Eq. (1), with a consequence that L_ϕ is r dependent [55]. L_ϕ was extracted for $V_g = +25$ V using the correlation field method [38] (see Fig. S1 in Ref. [56]). Although it decays with T, in particular above 200 mK, it remains of the same order of magnitude as the arms' length up to 500 mK, which confirms that our

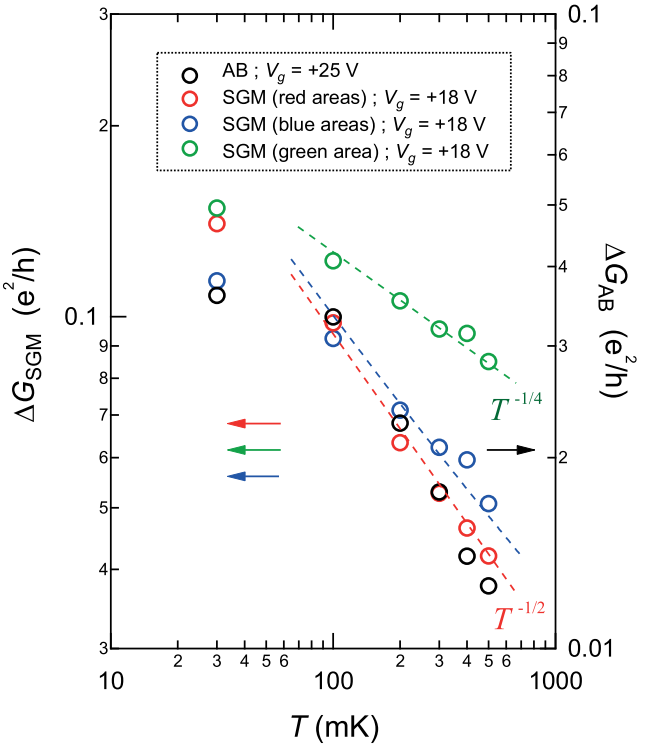

FIG. 6. (Color online) ΔG_{SGM} extracted from SGM maps calculated over the fluorinated areas enclosed by the red dashed boxes (red circles, left axis), in the regions where CB effects were evidenced at 500 mK enclosed by the blue dashed boxes (blue circles, left axis) and over the graphene QR area enclosed by the green dashed box (green circles, left axis) in Fig. 3(b) ($V_{tip} = -2$ V, $V_g = +18$ V, and $B = 0.7$ T). ΔG_{AB}, extracted from the magnetoconductance curves (black circles, right axis), vs T, for $V_g = +25$ V. Red and blue dashed lines are the result of a fit to $\alpha T^{-1/2} + \beta$ of ΔG_{SGM} calculated in the red ($\alpha = 0.94$ and $\beta = 0$) and blue ($\alpha = 0.94$ and $\beta = 0.0065$) boxes, respectively, in Fig. 3(b). The green dashed line is a fit to $\gamma T^{-1/4}$ ($\gamma = 0.4$) of ΔG_{SGM} calculated in the green box of Fig. 3(b).

sample is in the coherent regime of transport. The decay of L_ϕ above $T = 200$ mK is a likely explanation for the observation of a decrease of ΔG_{AB} faster than $T^{-1/2}$ in that range of temperature (see Fig. 6). Below 100 mK, the T dependence of ΔG_{SGM} in the SGM images deviates from $T^{-1/2}$ dependence. This observation is also found in the case of ΔG_{AB} calculated from the magnetoconductance data. We find that below $T \sim 80$ and ~50 mK, for $V_g = +18$ and +25 V, respectively, L_T becomes larger than the system size, as shown in Fig. S1 [56]. In this case, the term $L_T/\pi r$ disappears from Eq. (1) and ΔG_{AB} should saturate, as observed in Fig. 6.

Evaluating ΔG_{SGM} over the QR openings area [blue squares in Fig. 3(b)], i.e., in the regions where CB effects were evidenced at 500 mK, we find a weaker T dependence than in the AB-dominated area discussed above. This slower T dependence could be ascribed to an additional contribution from CB in the saturated regime [57]. Indeed, if CB were not in the saturated regime, a faster decay would be observed [39–41]. To test this hypothesis, we performed a fit of ΔG_{SGM} calculated on the QR openings to $\alpha T^{-1/2} + \beta$ (blue dashed line in Fig. 6), with the parameter α found from the fit to ΔG_{SGM} data obtained on the sides of the QR. This result copes with earlier experimental reports of low-temperature saturation of CB in graphene nanoribbons [57] and strengthens our interpretation of Gaussian features in Fig. 3(c) in terms of CB.

An even slower T dependence is found for ΔG_{SGM} calculated over the QR area, where quantum scars are observed [green square in Fig. 3(b)]. In this case, a good correspondence between the data and a fit to $\gamma T^{-1/4}$ is found. This T dependence corresponds to the decay expected for LDOS fluctuations in a quasi-one-dimensional geometry [4]. This is a further support for interpreting the SGM contrast as directly related to LDOS fluctuations when the tip scans above the QR area. The three distinct behaviors observed in Fig. 6 constitute a remarkable illustration of the ability of the SGM technique to separate the contributions of each physical phenomenon at play in such a complex nanostructure.

VII. CONCLUSION

In conclusion, we have used low-temperature scanning gate microscopy to image quantum and coherent transport in a diffusive graphene quantum ring fabricated thanks to a fluorination process. In the SGM images, we identified specific signatures of three different effects. First, from the observation of CB resonances, we find that active localized states are mainly concentrated close to the QR openings. Second, charge-carrier interferences were found to determine the SGM contrast when positioning the tip on the sides of the QR, evidencing an electrostatic AB effect. Third, radial conductance fringes are visible in SGM images when scanning the tip over the QR arms. These fringes are associated with resonant structures in the charge-carrier LDOS within the QR. Tight-binding simulations offer a support for the presence of such scars in a disordered quantum ring geometry. In summary, the real-space information yielded by SGM data allows us to bring a new light to the complex interplay of quantum and coherent effects that determine low-temperature transport in mesoscopic graphene devices. Noteworthy, since the quantum scars evidenced here were observed in a relatively disordered device, it is likely that analog scars can be found at low temperature in most graphene nanodevices currently discussed in the literature.

ACKNOWLEDGMENTS

This work was funded by the Fonds de la Recherche Scientifique FRS-FNRS (Grants No. T072.13 and No. FRFC2.4503.12) and by the Communauté Française de Belgique (ARC Grant No. 11/16-037, Project "Stresstronics"). D.C. is funded by a Fonds pour la Formation à la Recherche dans l'Industrie et dans l'Agriculture FRIA fellowship. F.M. and B.H. are FNRS research fellow and research associate, respectively. A.F. is a FNRS postdoctoral researcher.

[1] P. A. Lee and A. D. Stone, Phys. Rev. Lett. **55**, 1622 (1985).

[2] C. M. Marcus, A. J. Rimberg, R. M. Westervelt, P. F. Hopkins, and A. C. Gossard, Phys. Rev. Lett. **69**, 506 (1992).

[3] R. Akis, D. K. Ferry, and J. P. Bird, Phys. Rev. Lett. **79**, 123 (1997).

[4] A. D. Mirlin, Phys. Rep. **326**, 259 (2000).

[5] R. Crook, C. G. Smith, A. C. Graham, I. Farrer, H. E. Beere, and D. A. Ritchie, Phys. Rev. Lett. **91**, 246803 (2003).

[6] F. Martins, B. Hackens, M. G. Pala, T. Ouisse, H. Sellier, X. Wallart, S. Bollaert, A. Cappy, J. Chevrier, V. Bayot, and S. Huant, Phys. Rev. Lett. **99**, 136807 (2007).

[7] N. Aoki, R. Brunner, A. M. Burke, R. Akis, R. Meisels, D. K. Ferry, and Y. Ochiai, Phys. Rev. Lett. **108**, 136804 (2012).

[8] M. A. Eriksson, R. G. Beck, M. A. Topinka, J. A. Katine, R. M. Westervelt, K. L. Campman, and A. C. Gossard, Appl. Phys. Lett. **69**, 671 (1996).

[9] K. S. Novoselov, A. K. Geim, S. V. Morozov, D. Jiang, Y. Zhang, S. V. Dubonos, I. V. Grigorieva, and A. A. Firsov, Science **306**, 666 (2004).

[10] M. R. Connolly, K. L. Chiu, A. Lombardo, A. Fasoli, A. C. Ferrari, D. Anderson, G. A. C. Jones, and C. G. Smith, Phys. Rev. B **83**, 115441 (2011).

[11] N. Pascher, D. Bischoff, T. Ihn, and K. Ensslin, Appl. Phys. Lett **101**, 063101 (2012).

[12] A. G. F. Garcia, M. König, D. Goldhaber-Gordon, and K. Todd, Phys. Rev. B **87**, 085446 (2013).

[13] J. Martin, N. Akerman, G. Ulbricht, T. Lohmann, J. H. Smet, K. von Klitzing, and A. Yacoby, Nat. Phys. **4**, 144 (2008).

[14] J. Xue, J. Sanchez-Yamagishi, D. Bulmash, P. Jacquod, A. Deshpande, K. Watanabe, T. Taniguchi, P. Jarillo-Herrero, and B. J. LeRoy, Nat. Mat. **10**, 282 (2011).

[15] J. Berezovsky and R. M. Westervelt, Nanotechnology **21**, 274014 (2010).

[16] J. Berezovsky, M. F. Borunda, E. J. Heller, and R. M. Westervelt, Nanotechnology **21**, 274013 (2010).

[17] M. F. Borunda, J. Berezovsky, R. M. Westervelt, and E. J. Heller, ACS Nano **5**, 3622 (2011).

[18] S. Russo, J. B. Oostinga, D. Wehenkel, H. B. Heersche, S. S. Sobhani, L. M. K. Vandersypen, and A. F. Morpurgo, Phys. Rev. B **77**, 085413 (2008).

[19] J. S. Yoo, Y. W. Park, V. Skakalova, and S. Roth, Appl. Phys. Lett. **96**, 143112 (2010).

[20] D. Smirnov, H. Schmidt, and R. J. Haug, Appl. Phys. Lett. **100**, 203114 (2012).

[21] M. Huefner, F. Molitor, A. Jacobsen, A. Pioda, C. Stampfer, K. Ensslin, and T. Ihn, New J. Phys. **12**, 043054 (2010).

[22] Y. Nam, J. S. Yoo, Y. W. Park, N. Lindvall, T. Bauch, and A. Yurgens, Carbon **50**, 5562 (2012).

[23] A. Rahman, J. W. Guikema, S. H. Lee, and N. Markovic, Phys. Rev. B **87**, 081401 (2013).

[24] D. J. Mason, M. F. Borunda, and E. J. Heller, Phys. Rev. B **88**, 165421 (2013).

[25] L. Huang, Y.-C. Lai, D. K. Ferry, S. M. Goodnick, and R. Akis, Phys. Rev. Lett. **103**, 054101 (2009).

[26] H. Xu, L. Huang, Y.-C. Lai, and C. Grebogi, Phys. Rev. Lett. **110**, 064102 (2013).

[27] G. Bohra, R. Somphonsane, N. Aoki, Y. Ochiai, R. Akis, D. K. Ferry, and J. P. Bird, Phys. Rev. B **86**, 161405 (2012).

[28] A. Felten, A. Eckmann, J.-J. Pireaux, R. Krupke, and C. Casiraghi, Nanotechnology **24**, 355705 (2013).

[29] R. R. Nair, W. Ren, R. Jalil, I. Riaz, V. G. Kravets, L. Britnell, P. Blake, F. Schedin, A. S. Mayorov, S. Yuan, M. I. Katsnelson, H.-M. Cheng, W. Strupinski, L. G. Bulusheva, A. V. Okotrub, I. V. Grigorieva, A. N. Grigorenko, K. S. Novoselov, and A. K. Geim, Small **6**, 2877 (2010).

[30] J. T. Robinson, J. S. Burgess, C. E. Junkermeier, S. C. Badescu, T. L. Reinecke, F. K. Perkins, M. K. Zalalutdniov, J. W. Baldwin, J. C. Culbertson, P. E. Sheehan, and E. S. Snow, Nano Lett. **10**, 3001 (2010).

[31] F. Withers, M. Dubois, and A. K. Savchenko, Phys. Rev. B **82**, 073403 (2010).

[32] F. Withers, T. H. Bointon, M. Dubois, S. Russo, and M. F. Craciun, Nano Lett. **11**, 3912 (2011).

[33] H. Y. Liu, Z. F. Hou, C. H. Hu, Y. Yang, and Z. Z. Zhu, J. Phys. Chem. C **116**, 18193 (2012).

[34] W.-K. Lee, J. T. Robinson, D. Gunlycke, R. R. Stine, C. R. Tamanaha, W. P. King, and P. E. Sheehan, Nano Lett. **11**, 5461 (2011).

[35] A. Eckmann, A. Felten, A. Mishchenko, L. Britnell, R. Krupke, K. S. Novoselov, and C. Casiraghi, Nano Lett. **12**, 3925 (2012).

[36] A. M. Goossens, V. E. Calado, A. Barreiro, K. Watanabe, T. Taniguchi, and L. M. K. Vandersypen, Appl. Phys. Lett. **100**, 073110 (2012).

[37] B. Hackens, F. Martins, S. Faniel, C. A. Dutu, H. Sellier, S. Huant, M. Pala, L. Desplanque, X. Wallart, and V. Bayot, Nat. Commun. **1**, 39 (2010).

[38] Y.-F. Chen, M.-H. Bae, C. Chialvo, T. Dirks, A. Bezryadin, and N. Mason, J. Phys.: Condens. Matter **22**, 205301 (2010).

[39] K. Todd, H.-T. Chou, S. Amasha, and D. Goldhaber-Gordon, Nano Lett. **9**, 416 (2009).

[40] J. B. Oostinga, B. Sacépé, M. F. Craciun, and A. F. Morpurgo, Phys. Rev. B **81**, 193408 (2010).

[41] M. Y. Han, J. C. Brant, and P. Kim, Phys. Rev. Lett. **104**, 056801 (2010).

[42] Y. V. Nazarov, Physica B **189**, 57 (1993).

[43] B. Hackens, F. Martins, T. Ouisse, H. Sellier, S. Bollaert, X. Wallart, A. Cappy, J. Chevrier, V. Bayot, and S. Huant, Nat. Phys. **2**, 826 (2006).

[44] A. Pioda, S. Kicin, T. Ihn, M. Sigrist, A. Fuhrer, K. Ensslin, A. Weichselbaum, S. E. Ulloa, M. Reinwald, and W. Wegscheider, Phys. Rev. Lett. **93**, 216801 (2004).

[45] M. G. Pala, S. Baltazar, F. Martins, B. Hackens, H. Sellier, T. Ouisse, V. Bayot, and S. Huant, Nanotechnology **20**, 264021 (2009).

[46] C. W. Groth, M. Wimmer, A. R. Akhmerov, and X. Waintal, New J. Phys. **16**, 063065 (2014).

[47] M. G. Pala, B. Hackens, F. Martins, H. Sellier, V. Bayot, S. Huant, and T. Ouisse, Phys. Rev. B **77**, 125310 (2008).

[48] Note that the relative variance of LDOS fluctuations, calculated on the simulated LDOS, is ∼0.033 and ∼0.068 for Figs. 5(c) and 5(d), respectively. On the other hand, we know from [4] that the relative variance of the LDOS fluctuations inside a disordered metallic sample is of the order of $1/g$, where g is the dimensionless conductance. In our case, we evaluate $1/g \sim 0.044$ and ∼0.059, from the conductance simulated with the parameters of Figs. 5(c) and 5(d), respectively. The relative variance and $1/g$ are indeed of the same order of magnitude, in agreement with the theory .

[49] S. B. Touski and M. Pourfath, Appl. Phys. Lett. **103**, 143506 (2013).

[50] M. Ishigami, J. H. Chen, W. G. Cullen, M. S. Fuhrer, and E. D. Williams, Nano Lett. **7**, 1643 (2007).

[51] S. Washburn, C. P. Umbach, R. B. Laibowitz, and R. A. Webb, Phys. Rev. B **32**, 4789 (1985).
[52] F. P. Milliken, S. Washburn, C. P. Umbach, R. B. Laibowitz, and R. A. Webb, Phys. Rev. B **36**, 4465 (1987).
[53] T. Chwiej and B. Szafran, Phys. Rev. B **87**, 085302 (2013).
[54] S. Washburn and R. A. Webb, Adv. Phys. **35**, 375 (1986).
[55] T. Ludwig and A. D. Mirlin, Phys. Rev. B **69**, 193306 (2004).
[56] See Supplemental Material at http://link.aps.org/supplemental/10.1103/PhysRevB.90.205433 for calculation results of the thermal diffusion length and of the coherence length. A detailed description of the calculation method is also presented.
[57] S. Dröscher, H. Knowles, Y. Meir, K. Ensslin, and T. Ihn, Phys. Rev. B **84**, 073405 (2011).